

Cite this: DOI: 10.1039/c0xx00000x

www.rsc.org/xxxxxx

ARTICLE TYPE

# Polypyrrole-derived Mesoporous Nitrogen-doped Carbons with Intrinsic Catalytic Activity in the Oxygen Reduction Reaction

Marta Sevilla,<sup>\*a</sup> Linghui Yu,<sup>b</sup> Tim Patrick Feller,<sup>b</sup> Antonio B. Fuertes,<sup>a</sup> Maria-Magdalena Titirici<sup>c</sup><sup>5</sup> Received (in XXX, XXX) Xth XXXXXXXXX 20XX, Accepted Xth XXXXXXXXX 20XX

DOI: 10.1039/b000000x

N-doped mesoporous carbons containing small amounts of graphitic carbon have been successfully prepared using the nanocasting technique. Polypyrrole was used as N-dopant carbon precursor and SBA-  
10 15 or silica xerogel as templates. Graphitic carbon domains provide a good electronic conductivity of up to  $0.33 \text{ S cm}^{-1}$ , a necessary property for electrochemical applications, while a mesoporous structure reduces mass transport limitations. These characteristics are further combined with a high N content (3.55 – 5.45 wt.%). As a result, the as-prepared materials exhibit an enhanced intrinsic electrocatalytic activity towards the oxygen reduction reaction (ORR). They exhibit an onset potential of  $\sim -90$  to  $-70 \text{ mV vs.}$   
15 Ag/AgCl and a current density in the lower potential regime that exceeds that of a commercial platinum catalyst in a basic medium. Their behavior is superior to that of Vulcan XC72R carbon. Furthermore, unlike commercial Pt catalysts, they are unaffected by the methanol cross-over effect. It was found that the graphitic content must be well-balanced as, on the one hand, it enhances conductivity but, on the other hand, it selectively catalyses an unfavorable  $2\text{e}^-$  process.

## 20 Introduction

Nitrogen-containing carbons have attracted increasing interest among the scientific community over the past few years as they improve the properties of bulk carbon for use in various applications. The incorporated nitrogen functional groups have a  
25 deep effect on the carbon properties. In particular, electrical conductivity, basicity, oxidation stability, and catalytic activity are directly affected and often enhanced when nitrogen is introduced into the carbon structure.<sup>1,2</sup>

The performance of these materials is strongly dependent on  
30 the amount of nitrogen in the carbon host as well as on its local structure. Nitrogen-doping in carbon materials can be performed either directly during synthesis or by post-synthetic treatment. However, post-treatment methodologies often yield only surface functionalization.<sup>3-5</sup> The bulk material properties are not affected.  
35 In contrast, “in situ” doping during solid synthesis using nitrogen-containing precursors ensures the homogeneous incorporation of nitrogen throughout the entire carbon material. Several N-doped carbons have been prepared using this method. For example, high surface area porous carbons with a high nitrogen content have  
40 been synthesized by means of cyclotrimerization reactions between carbonitriles and cyano-containing ionic liquids under ionothermal conditions,<sup>6-10</sup> and by nanocasting or chemical activation using as carbon precursor N-containing organic compounds<sup>11,12</sup> or mixtures of nitrogen-containing compounds  
45 (i.e. melamine, urea, etc) and N-free materials.<sup>13</sup> Furthermore, N-doped CNTs and CNFs have been synthesized by methods similar to that used to synthesize bulk CNTs, but using precursors such as melamine,<sup>14</sup> benzylamine,<sup>15</sup> acetonitrile,<sup>16</sup> N-

heterocycles,<sup>17,18</sup> phthalocyanines,<sup>18</sup> and again specific ionic  
50 liquids.<sup>19</sup>

Bulk nitrogen-doped carbons have been commonly investigated as metal-free catalysis for the electrochemical oxygen reduction reaction (ORR). This reaction takes place in the cathodic compartment of polymer-electrolyte membrane fuel  
55 cells, membrane-reactors for the production of hydrogen peroxide and metal-air batteries.<sup>2,8,20,21</sup> There is a great interest in to replace the expensive fuel cell electrodes containing supported noble metals such as Pt and Ru. In this sense, it was found that metal phthalocyanine complexes exhibit a certain catalytic  
60 activity in ORR.<sup>22</sup> Such complexes are known to be the catalytically active centers of redox-active enzymes. Other metal macrocycles, such as metalloporphyrins, have also been selected as cathode catalysts for ORR.<sup>23</sup> To increase the stability and durability of these catalysts during the electrochemical operation,  
65 these complexes have been further pyrolyzed, yielding carbon structures doped with nitrogen and metals.<sup>24-26</sup> These carbons have also shown increased electrocatalytic activity.

An important step towards the practical fabrication of fuel cells was achieved with the replacement of the expensive  
70 phthalocyanine precursor by cheaper precursors, such as polyacrylonitrile.<sup>27</sup> However, the greatest advancement has been the demonstration that metal-free catalysis using N-doped carbon materials is possible. Thus, Gong et al. proved that vertically aligned N-containing CNTs can catalyze oxygen reduction in an  
75 alkaline medium, providing a better performance than Pt.<sup>28</sup> Similarly, Liu et al. prepared N-doped ordered mesoporous graphitic arrays using a metal-free nanocasting technique with an electrochemical performance superior to that observed with a

commercially available Pt-C catalyst.<sup>11</sup> Further advancements in the development of cheap and sustainable fuel cells rely with the use of economic and environmentally-friendly catalyst precursors.

The catalytic mechanism of ORR is a matter of discussion especially regarding the role of the metal nanoparticles and the nitrogen within the structures.<sup>29</sup> The main hypotheses concerning the mode of operation are briefly summarized as follows: (1) the metal nanoparticles are the catalytically active sites, which through thermal treatment become well-dispersed, so enhancing their catalytic activity; (2) the catalytically active centers are the metal nanoparticles, which are influenced by the surrounding carbon and nitrogen atoms; (3) the metal nanoparticles just promote the formation of the catalytically active center in the C/N-system, but have no catalytic function during the ORR. To date, none of these hypotheses have been proven as exclusively valid. It is speculated that the catalytic mechanism of ORR may involve elements from all three hypotheses, which would explain the controversial analysis of similar experimental findings. However, it is generally accepted that the nitrogen incorporated into the structures plays a key role in the catalytic function.<sup>28, 30-32</sup>

The role of the nitrogen in the ORR reaction is not fully understood but a major contribution is attributed to the pyridinic nitrogen atoms on the edges of the graphitic planes.<sup>31-33</sup> On these sites, oxygen activation can be expected to occur at C-sites in the proximity of the nitrogen atoms.<sup>34</sup> Furthermore, it is unclear why some N-doped carbons catalyze the two-electron mechanism and others the four-electron mechanism.<sup>8, 9</sup> On the other hand, theoretical studies show that the polarization of the C-N bond of quaternary nitrogen leads to increased interaction between the adjacent carbon atoms and the oxygen radicals, which induces enhanced catalytic activity.<sup>35</sup> Depending on the surface nitrogen density, other electron mechanisms may be favored.<sup>34</sup>

Among the precursors used for the synthesis of N-doped carbons, polymers such as polyacrylonitrile and polypyrrole stand out for their high nitrogen content, high carbon yield when pyrolyzed and low-cost.<sup>36, 37</sup> Atanassov et al. studied the oxygen reduction reaction (ORR) processes in alkaline media on a family of electrocatalyst materials derived from a Co-containing precursor and a polypyrrole-carbon composite material (PPy/C). The effects of Co loading and heat treatment temperature on the CoPPy/C materials were revealed through structural evaluations and electrochemical studies. The authors proposed that the ORR mechanism occurs in this class of non-platinum based fuel cell cathode catalysts through dual site functionality where O<sub>2</sub> is initially reduced at a Co<sup>2+</sup>-containing N-C type site in a 2e<sup>-</sup> process to form HO<sub>2</sub><sup>-</sup>, an intermediate reaction product which may further react at the decorating Co<sub>x</sub>O<sub>y</sub>/Co surface nanoparticle phase. Shrestha and Mustain analysed the behaviour in the ORR process of metal-free polypyrrole-derived N-doped mesoporous carbons prepared by a nanocasting method.<sup>38</sup> The iron salt used as polymerization catalyst was removed prior to carbonization, so that the final carbon material exhibited a low level of graphitization. This material displayed a higher catalytic activity and lower activation overpotential in the ORR reaction than Vulcan XC-72R.

Here, we have synthesized N-doped mesoporous carbons

containing small quantities of graphitized carbon by means of the nanocasting technique using polypyrrole as carbon precursor. The graphitic domains were generated by the catalytic action of the iron nanoparticles produced during the carbonization process through the carbothermal reduction of the iron salt employed as polymerization catalyst. In this way, materials combining a high surface area ( $S_{\text{BET}} \sim 1000 - 1500 \text{ m}^2 \text{ g}^{-1}$ ), an accessible mesoporous structure, a high nitrogen content (3.6 – 5.5 wt%) and an improved electronic conductivity were obtained. The catalytic properties of these materials in the oxygen reduction reaction were investigated in both acid and basic media.

## Experimental

### Synthesis of silica and templated carbons

Two mesoporous silica materials, SBA-15 and silica xerogel (SX), were used as templates for the preparation of the mesoporous carbon materials. Both silica materials were synthesized according to the procedures reported by Fuertes.<sup>39, 40</sup> The synthesis of the carbon materials was carried out as follows: i) infiltration of the silica porosity up to incipient wetness with a solution of 1.5 M of FeCl<sub>3</sub> in ethanol, ii) infiltration up to incipient wetness of the dried FeCl<sub>3</sub>-impregnated silica with pyrrole (recently distilled under N<sub>2</sub>), iii) chemical polymerization of pyrrole and its conversion into polypyrrole (PPy) (16h at room temperature), iv) carbonization of the silica-PPy nanocomposite under N<sub>2</sub> at 900 °C (1h) and v) removal of the template by HF (48 %). These samples were denoted as CS900 (with SBA-15 as template) and CX900 (with silica xerogel as template). Another carbon sample, denoted as CX1000 (with silica xerogel as template), was prepared as described above except that the carbonization temperature was 1000 °C.

### Characterization

X-ray diffraction (XRD) patterns at small and wide angles were obtained on a Siemens D5000 instrument operating at 40 kV and 20 mA, using Cu K $\alpha$  radiation ( $\lambda = 0.15406 \text{ nm}$ ). Nitrogen physisorption isotherms were performed at -196°C on a Micromeritics ASAP 2010 volumetric adsorption system. The BET surface area was determined from an analysis of the isotherms in the relative pressure range of 0.04 to 0.20. The total pore volume was calculated from the amount adsorbed at a relative pressure of 0.99. The PSD was calculated by means of the Kruk-Jaroniec-Sayari method (KJS)<sup>41</sup> applied to the adsorption branch. Transmission electron microscopy (TEM) images were taken on a JEOL (JEM-2000 FX) operating at 200 kV. X-ray photoelectron spectroscopy (XPS) was carried out on a Specs spectrometer, using MgK $\alpha$  (1253.6 eV) radiation from a double anode at 50 w. The binding energies for the high-resolution spectra were calibrated by setting C 1s to 284.6 eV. The Raman spectra were recorded by using a Horiva (LabRam HR-800) spectrometer. The source of radiation was a green laser operating at a wavelength of 514 nm and a power of 25 mW. Elemental analysis CHN was carried out on a LECO CHN-932 microanalyzer. The electronic conductivity of the carbon powders was determined by pressing them between two plungers into a hollow Nylon cylinder (inner diameter of 8 mm), and applying a pressure of up to 7.1 MPa. Thermogravimetric analysis of the

carbon samples was carried out in a CI Electronics system.

### Electrochemical oxygen reduction reaction (ORR)

To perform electrochemical testing, a standard ink was prepared by mixing 5 mg of catalyst with 95  $\mu\text{L}$  Nafion® binder solution and 350  $\mu\text{L}$  of ethanol. The ink was ultrasonicated for at least 30 minutes for homogenization. A 5  $\mu\text{L}$  aliquot was dropped onto a freshly polished glassy carbon rotating disk electrode (diameter  $\sim 5$  mm, electrode area 0.196  $\text{cm}^2$ ) to prepare a thin film. When necessary, the electrode was heated to  $\sim 50$   $^\circ\text{C}$  in an oven prior to the application of ink in order to achieve better electrode coverage of the catalyst film. Vulcan® XC72R (Cabot Corporation) and a commercial Pt@C catalyst (20% Pt on carbon black, Alfa Aesar) were also analyzed for comparison. Electrochemical tests were performed in 0.1 M KOH or 0.05 M  $\text{H}_2\text{SO}_4$  in a standard three-electrode setup fitted with an Ag/AgCl reference electrode using Gamry Reference 600 potentiostat (Gamry Instruments) and Gamry EIS 300/Physical Electrochemistry software. The current values obtained were normalized to the mass of the catalyst used (*i.e.* given in  $\text{mA mg}^{-1}$ ) to allow direct comparison between samples. For the Koutecky-Levich analysis, the unnormalized currents obtained from measurements at varying rotation rates (400, 800, 1200, 1600, 2000, and 2500 rpm) were used.

The Levich current,  $I_{\text{lev}}$ , is given by:  $I_{\text{lev}} = 0.62nFAD^{2/3}\omega^{1/2}\nu^{-1/6}C$ , being  $n$  = number of electrons transferred in the half reaction,  $F$  = Faraday constant,  $A$  = electrode area,  $D$  = diffusion coefficient of the reactant in the electrolyte,  $\omega$  = angular rotation rate of the electrode,  $\nu$  = kinematic viscosity of the electrolyte and  $C$  = analyte concentration.

The kinetic current,  $I_k$  is given by:  $I_k = nFAkC\Gamma_{\text{cat}}$ , being:  $n$  = number of electrons transferred in the half reaction,  $F$  = Faraday constant,  $A$  = electrode area,  $k$  = pseudo-second order rate constant,  $C$  = analyte concentration and  $\Gamma_{\text{cat}}$  = catalyst loading.

The combination of both equations leads to the Koutecky-Levich expression, which describes the overall RDE limiting current  $I_{\text{lim}}$  for the electrocatalytic reaction over the entire potential range:  $1/I_{\text{lim}} = 1/I_k + 1/I_{\text{lev}}$

The Koutecky-Levich plot of  $1/I_{\text{lim}}$  against  $1/\omega^{1/2}$  should yield a straight line whose slope is related to the number of electrons transferred in the reaction, and whose intercept is related to the kinetic current.

## Results and discussion

### Structural and chemical properties of the carbons

Complete information about the preparation methods and the structural characteristics of the silica materials are given elsewhere.<sup>39, 40</sup> SBA-15 is an ordered mesostructured silica with uniform pores of  $8 \pm 1$  nm. In contrast, the silica xerogel possesses disordered porosity and consequently a broader pore size distribution (PSD), in the 3 – 20 nm range. These silica materials were used as hard templates for the production of the polypyrrole mesoporous carbons. Fig. 1 shows TEM images of CS900 and CX1000. Figs. 1a and 1b, which were taken along and perpendicular to the channel direction respectively, evidence that the structural order of SBA-15 is preserved in its carbon replica

CS900. It exhibits the structure typical of CMK-3 carbon, *i.e.* well-ordered hexagonal arrays of carbon nanorods connected by means of carbon spacers. The low-angle XRD pattern of this sample (Fig. S1 in SI) shows the characteristic (100) peak, which is consistent with a high degree of hexagonal mesoscale organization and therefore successful replication of SBA-15. On the other hand, Fig. 1c shows a highly disordered pore network, typical of silica xerogel. Thus, CX900 (image not shown) and CX1000 have also inherited the structural characteristics of the template. A more detailed analysis of the porous characteristics of the samples was obtained by  $\text{N}_2$  physisorption, the results of which are collected in Table 1 and Fig. 2. All the templated carbons possess a two-step isotherm (Fig. 2a), which indicates a bimodal PSD. This is confirmed by the PSDs shown in Fig. 2b. The pore system centred at 3 nm for CS900 and 4 nm for CX900 and CX1000, correspond to mesopores generated from the dissolution of the silica framework, whereas the pore system with maxima at  $\geq 10$  nm is formed by the coalescence of the non-filled silica pores with those resulting from the removal of the silica walls.<sup>42</sup> The PSD of this pore system is broader because it depends on the number of adjacent non-filled silica pores that are involved. All the templated carbons possess a BET surface area larger than 1000  $\text{m}^2 \text{g}^{-1}$  and a pore volume of up to 2.1  $\text{cm}^3 \text{g}^{-1}$ . These textural characteristics are superior to those reported by Shrestha and Mustain for polypyrrole-derived N-doped mesoporous carbons.<sup>38</sup>

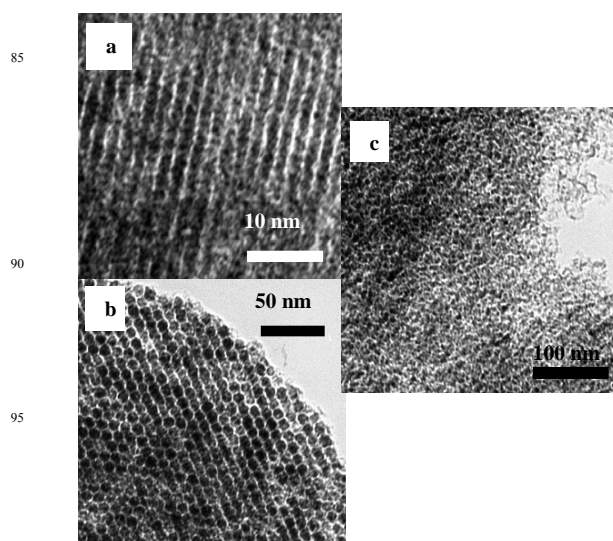


**Fig. 1.** TEM micrographs of templated PPy-carbons: CS900 (a and b), and CX1000 (c).

Fig. 3a shows the XRD patterns in the wide-angle region for the PPy-based carbons. A sharp peak can be observed at  $2\theta = 26.5^\circ$ , which corresponds to the (002) diffraction peak of graphite. This peak is superimposed on a broad profile corresponding to amorphous carbon, which reveals that the material is composed of a matrix of amorphous carbon with small quantities of graphitised carbon. This result is further supported by the Raman analysis of different areas of the samples. Thus, a clear dependence of the shape of the Raman spectra on the focused area was recorded. All local spectra exhibited the two characteristic D and G bands, which usually were rather broad,

which is indicative of amorphous carbon (Fig. S2a in SI). In some focused areas, the presence of a strong and sharp G-band at 1575  $\text{cm}^{-1}$  and a weak D-band at 1345  $\text{cm}^{-1}$  could be observed. Together with the reduced D/G intensity ratio (a measure of the degree of order in carbons), these signals can be assigned to graphitized areas. The percentage of graphitic carbon is around 8–9 wt.% as determined by means of thermogravimetric analysis (see Fig. S2b in SI). These graphitic domains are generated close to the iron nanoparticles that act as a graphitization catalyst and that were previously formed during the carbonization process *via* the carbothermal reduction of the iron salt employed as polymerization catalyst.<sup>43</sup> As a consequence of the presence of these graphitic domains, the PPy-derived carbons exhibit electronic conductivities in the 0.03–0.33  $\text{S cm}^{-1}$  range, values which are one to two orders of magnitude greater than those of amorphous templated carbons.<sup>37, 43, 44</sup>

**Table 1.** Physical and chemical properties of silica samples and templated carbons.

Sample	$S_{\text{BET}}$ ( $\text{m}^2 \text{g}^{-1}$ )	$V_p$ ( $\text{cm}^3 \text{g}^{-1}$ )	Pore size (nm) <sup>a</sup>	Electrical conductivity ( $\text{S cm}^{-1}$ )	N (wt.%)
SBA-15	940	1.2	8.2	-	-
SX	510	0.8	8.6	-	-
CS900	1170	1.3	3.0/10	0.03	5.45
CX900	1060	1.5	4.0/22	0.33	4.91
CX1000	1480	2.1	4.3/10	0.21	3.55

<sup>a</sup> Maximum or maxima of the PSD

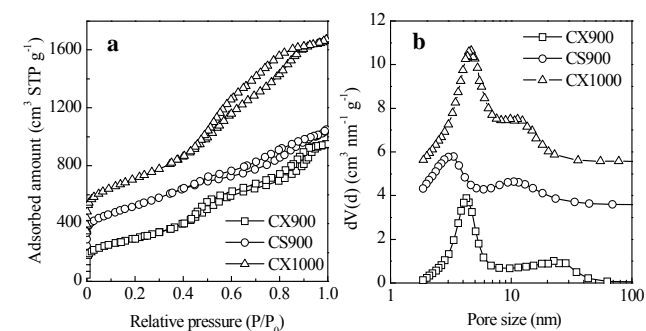


**Fig. 2.** a)  $\text{N}_2$  physisorption isotherms and b) pore size distributions of the templated carbons. For sake of clarity, the isotherms of CS900 and CX1000 in Fig. 2a have been shifted up by 200 and 300  $\text{cm}^3 \text{g}^{-1}$  respectively. The PSDs in Fig. 2b have also been shifted up.

Another appealing characteristic of these materials is the presence of a high proportion of N, i.e. 3.6 – 5.5 wt.% left by the pyrrole precursor. As mentioned in the introduction, N-doped porous materials have recently attracted great interest in relation to the cathodic oxygen-reduction reaction (ORR) in fuel cells due to their excellent electrocatalytic activity, long-term stability and excellent resistance to cross-over effects.<sup>11, 45, 46</sup> It is believed that pyridinic groups play the most important role in the ORR reaction, although this is still open to discussion. Therefore, not only the amount of nitrogen, but also the type of N-structures present, is an important issue. To analyse the N-containing species in the mesoporous carbons, XPS analyses were

performed. The high-resolution N 1s core level spectrum for CX900 is shown in Fig. 3b. Four contributions can be distinguished, as indicated in Fig. 3b: i) pyridinic-N at 398.3 eV, ii) pyrrolic/pyridonic-N at 399.7 eV, iii) quaternary-N at 401 eV and iv) pyridine-N oxides at 402.5 eV. The main contribution corresponds to quaternary-N, followed by pyrrolic/pyridonic and pyridinic N.

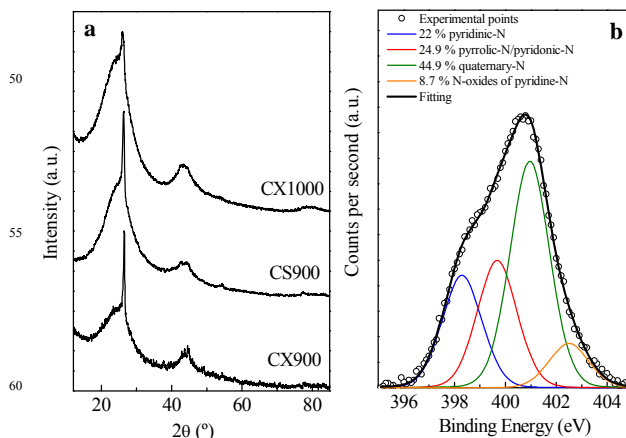


**Fig. 3.** a) XRD patterns corresponding to the mesoporous carbons and b) N 1s core level spectrum of CS900.

#### Electrocatalytic activity for oxygen reduction reaction

The N-doped CS900, CX900 and CX1000 samples were tested for their electrocatalytic activity in the oxygen reduction reaction (ORR). Cyclic voltammetry (CV) at a scan rate of 50  $\text{mV s}^{-1}$  and rotating disk electrode (RDE) linear sweep voltammetry (LSV) at a scan rate of 10  $\text{mV s}^{-1}$  were conducted in 0.1 M KOH. The results of the electrochemical testing in 0.05 M  $\text{H}_2\text{SO}_4$  are available in the supporting information (Figs. S3 and S4). CVs, performed in  $\text{N}_2$ -saturated solution, led to reversible curves with very broad features for all N-doped carbons in both acid and basic media (Fig. 4a). These signals are characteristic of heteroatom doped carbons measured in an aqueous environment. In the case of the acidic medium, the shoulder is due to the (de)protonation of N sites and is a little more distinct, though still very broad. The almost rectangular corners of the voltammograms indicate the high electronic conductivity, as pointed out above, as well as good charge propagation throughout the mesoporosity. The large area under the curves, which arises from capacitive currents, underlines the high surface area of the porous electrodes. In contrast, a well-defined cathodic peak at -0.179 V for CS900 and a shoulder for CX900 and CX1000, appears in the  $\text{O}_2$ -saturated 0.1 M KOH solution, clearly demonstrating the electrocatalytic activity of the N-doped porous carbons towards oxygen reduction (Fig. 4b). This value is positively shifted by 13 mV in comparison to high surface area N-doped mesoporous carbons made from ionic liquids and nucleobases,<sup>9</sup> and by 81 mV compared to N-doped ordered amorphous graphitic arrays prepared from a N-containing aromatic dyestuff.<sup>11</sup> This result already points out the good electrocatalytic behavior towards ORR of these materials. On the other hand, it is commonly remarked in the literature that N-

doped carbons are less active in acidic than in alkaline media. Thus, the pronounced cathodic peaks found in 0.1 M KOH are not visible in 0.05 M H<sub>2</sub>SO<sub>4</sub> at the same scan rate of 50 mV s<sup>-1</sup> (see Fig. S3 in SI).

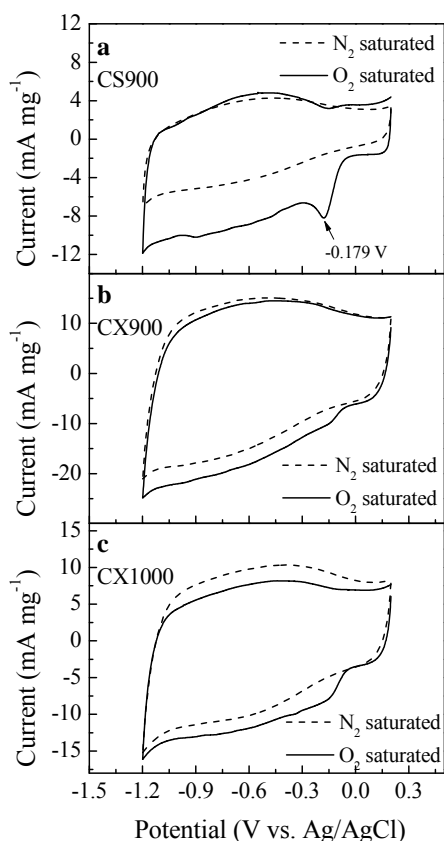


**Fig. 4.** Cyclic voltammograms of the mesoporous carbons at a scan rate of 50 mV s<sup>-1</sup> in 0.1 M KOH.

The polarization curves obtained from RDE (1600 rpm) linear sweep voltammetry in O<sub>2</sub>-saturated 0.1 M KOH are shown in Fig. 5a (the corresponding curves in 0.05 M H<sub>2</sub>SO<sub>4</sub> are presented in Fig. S4 in SI). A summary of values derived from the plots is given in Table 2.

In 0.05 M H<sub>2</sub>SO<sub>4</sub>, both the onset potential and maximum current density have significantly improved for all the N-doped carbons relative to pure Vulcan. Compared to Pt@C, however, these materials are still not competitive. In 0.1 M KOH, the performance of the N-doped materials is much more pronounced. As in the acidic medium, the performance of the N-doped carbons clearly exceeds that of Vulcan carbon. Compared to the commercial Pt catalyst, a cathodic shift of the onset potential of ~130 mV can be observed. This is a relatively high overpotential, also compared to the N-doped carbon nanotube catalysts reported by Gong *et al.*<sup>28</sup> However, the limited currents in the lower potential regime exceed the ones of the commercial platinum catalyst. This clearly shows that the option to structurally tailor N-doped carbon catalysts can be used to partially outperform chemically much more active, but at the same time, much more expensive electrocatalysts. The well-designed porosity reduces mass-transport related limitations, whereas the high density of catalytically active sites reduces kinetic limitations.

**Table 2.** Summary of values derived from Linear Sweep Voltammetry and Chronoamperometry measurements using a Rotating Disk Electrode in O<sub>2</sub>-saturated 0.05 M H<sub>2</sub>SO<sub>4</sub> and 0.1 M KOH. All the potentials are given vs. Ag/AgCl.

Sample	0.1 M KOH		0.05 M H <sub>2</sub> SO <sub>4</sub>	
	Onset potential (mV) <sup>a</sup>	Max. current density (mA mg <sup>-1</sup> ) / Corresponding voltage (mV)	Onset potential (mV) <sup>a</sup>	Max. current density (mA mg <sup>-1</sup> ) / Corresponding voltage (mV)
CS900	-94	18.7 / -1081	363	14.4 / -200
CX900	-77	20.7 / -1061	469	13.9 / -200
CX1000	-73	20.2 / -1024	413	13.7 / -200
Vulcan	-183	13.9 / -911	-36	3.4 / -200
Pt@C	55	17.1 / -754	540	16.7 / -200

<sup>a</sup> The onset potential is defined as the value of potential at which the current reaches 10% of the maximum value.

A Koutecky-Levich analysis of the N-doped carbon catalysts was carried out. The results at a potential of -0.3 V vs. Ag/AgCl are shown in Fig. 5b. It can be seen that CS900 (*n* = 3.94), CX900 (*n* = 3.2) and CX1000 (*n* = 3.45), all have electron transfer numbers lower than four, indicating a mixed mechanism due to the different catalytic sites. It is a well-known fact that graphite catalyzes the two-electron mechanism. We may therefore conclude that the mixed processes occur due to the combined contribution of N-doped carbon and graphitic carbon areas, both of which are present in all the samples as shown by XRD. In fact, CS900 is very close to a pure 4e<sup>-</sup> process, which we ascribe to the fact that it possesses the lowest amount of graphitic carbon. That it has the smallest graphite content is confirmed by the fact that it has the highest nitrogen content compared with the xerogel-templated CX samples and the lowest -though still sufficient- conductivity. For CX900 and CX1000, the differences in activity and electron transport number are rather small. However, CX1000 shows a slightly better electrocatalytic performance and is closer to a four-electron mechanism, indicating a stronger contribution by the N-doped areas. As pointed out in the introduction, N-doped carbons often enhance their catalytic performance at higher synthesis temperatures, even though the N content is reduced. As can be observed from XRD and the values for electrical conductivity, graphitic carbon content however is also smaller compared to CX900 resulting in a larger electron transfer number.

One of the main drawbacks of the platinum catalyst in current direct methanol fuel cell systems is its sensitivity towards the so-called methanol cross-over effect. To compare the stability of the electrocatalysts, the chronoamperometric response on injecting methanol into the O<sub>2</sub>-saturated electrolyte at a polarization of -0.26 V vs. Ag/AgCl was measured in 0.1 M KOH (Fig. 5c). Both CX1000 and Pt@C show ORR activity from the moment of oxygen bubbling (*t* = 1051s). With the injection of methanol (*t* = 2101s), a rapid degradation of the platinum catalyst can be observed, indicated by the dramatic loss of cathodic current. In contrast, CX1000 does not show any sensitivity towards the presence of methanol and the cathodic current remains completely stable, making the advantage of N-doped carbon catalysts abundantly clear.

Cite this: DOI: 10.1039/c0xx00000x

www.rsc.org/xxxxxx

ARTICLE TYPE

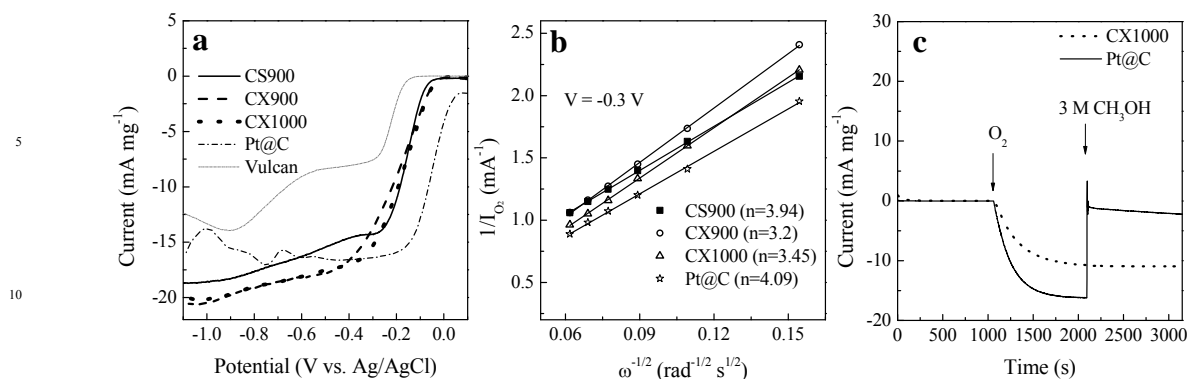


**Fig. 5.** a) RDE polarization curves of the mesoporous carbons, Vulcan carbon, and 20 wt% Pt@C in 0.1 M KOH at a constant rotation rate of 1600 rpm. b) Koutecky-Levich plots of the mesoporous carbons in 0.1 M KOH at -0.3 V. c) Current-time (i-t) response of CX1000 and the Pt@C at -0.26 V in 0.1 M KOH saturated with N<sub>2</sub> (0-1050 s) or O<sub>2</sub> (1051-2100 s) and in O<sub>2</sub>-saturated 3 M CH<sub>3</sub>OH (2101-3150 s).

## Conclusions

N-doped mesoporous carbons containing small amounts of graphitic carbon with surface areas in the 1000 – 1500 m<sup>2</sup> g<sup>-1</sup> range and N contents in the 3.55 – 5.45 wt.% range, have been successfully prepared by the nanocasting technique using polypyrrole as N-dopant carbon precursor and SBA-15 and silica xerogel as templates. The carbon materials are faithful replicas of the templates, exhibiting the well-ordered hexagonal structure of SBA-15 or the highly disordered pore network of the silica xerogel. A fraction of amorphous carbon is converted into graphitic carbon due to the catalytic action of the Fe nanoparticles generated during the carbonization process. The graphitic domains confer on the carbon materials a good electronic conductivity. The N-doped carbons which were used in the oxygen reduction reaction (ORR) showed an enhanced intrinsic electrocatalytic activity. Thus, the overpotential of ORR reaction is much lower than that of Vulcan XC-72R, and the current density in the lower potential regime exceeds that of a commercial platinum catalyst. What is more, they show no sensitivity towards the methanol cross-over effect, unlike the commercial platinum catalyst. It is, therefore, clearly shown that the option to structurally tailor N-doped carbon catalysts can be used to partially outperform chemically much more active, but at the same time much more expensive electrocatalysts. The well-designed porosity reduces mass-transport limitations, whereas the high density of catalytically active sites reduces kinetic limitations.

## Acknowledgements

The financial support for this research work provided by the Spanish MCyT (MAT2012-31651) is gratefully acknowledged.

M. S. thanks the Spanish MCyT for the award of a Ramón y Cajal contract.

## Notes and references

- <sup>a</sup> Instituto Nacional del Carbón (CSIC), P.O. Box 73, Oviedo 33080, Spain.
- <sup>b</sup> Max-Planck Institute of Colloids and Interfaces, Am Mühlenberg 1, 14476, Potsdam, Germany
- <sup>c</sup> Queen Mary University of London, School of Engineering and Materials Science, Mile End Road, E1 4NS, London
- † Electronic Supplementary Information (ESI) available: [details of any supplementary information available should be included here]. See DOI: 10.1039/b000000x/
- ‡
- §
1. C. P. Ewels and M. Glerup, *Journal of Nanoscience and Nanotechnology*, 2005, **5**, 1345-1363.
2. Y. Shao, J. Sui, G. Yin and Y. Gao, *Applied Catalysis B: Environmental*, 2008, **79**, 89-99.
3. L. Jiang and L. Gao, *Carbon*, 2003, **41**, 2923-2929.
4. S. C. Roy, A. W. Harding, A. E. Russell and K. M. Thomas, *Journal of the Electrochemical Society*, 1997, **144**, 2323-2328.
5. M.-M. Titirici, A. Thomas and M. Antonietti, *Journal of Materials Chemistry*, 2007, **17**, 3412-3418.
6. P. Kuhn, A. I. Forget, D. Su, A. Thomas and M. Antonietti, *Journal of the American Chemical Society*, 2008, **130**, 13333-13337.
7. J. S. Lee, X. Wang, H. Luo, G. A. Baker and S. Dai, *Journal of the American Chemical Society*, 2009, **131**, 4596-4597.
8. T. P. Fellingner, F. Hasche, P. Strasser and M. Antonietti, *Journal of the American Chemical Society*, 2012, **134**, 4072-4075.
9. W. Yang, T. P. Fellingner and M. Antonietti, *Journal of the American Chemical Society*, 2011, **133**, 206-209.
10. J. P. Paraknowitsch, J. Zhang, D. Su, A. Thomas and M. Antonietti, *Advanced Materials*, 2010, **22**, 87-92.



11. R. Liu, D. Wu, X. Feng and K. Müllen, *Angew. Chem. Int. Ed.*, 2010, **49**, 2565-2569.
12. M. Sevilla, R. Mokaya and A. B. Fuertes, *Energy & Environmental Science*, 2011, **4**, 2930-2936.
13. K.-S. Kim and S.-J. Park, *Electrochim. Acta*, 2011, **56**, 10130-10136.
14. M. Terrones, P. Redlich, N. Grobert, S. Trasobares, W.-K. Hsu, H. Terrones, Y.-Q. Zhu, J. P. Hare, C. L. Reeves, A. K. Cheetham, M. Rühle, H. W. Kroto and D. R. M. Walton, *Advanced Materials*, 1999, **11**, 655-658.
15. M. Terrones, R. Kamalakaran, T. Seeger and M. Rühle, *Chemical Communications*, 2000, 2335-2336.
16. A. G. Kudashov, A. V. Okotrub, L. G. Bulusheva, I. P. Asanov, Y. V. Shubin, N. F. Yudanov, L. I. Yudanova, V. S. Danilovich and O. G. Abrosimov, *The Journal of Physical Chemistry B*, 2004, **108**, 9048-9053.
17. D. P. Kim, C. L. Lin, T. Mihalisin, P. Heiney and M. M. Labes, *Chemistry of Materials*, 1991, **3**, 686-692.
18. L. Zhi, T. Gorelik, R. Friedlein, J. Wu, U. Kolb, W. R. Salaneck and K. Müllen, *Small*, 2005, **1**, 798-801.
19. X. Tuaev, J. P. Paraknowitsch, R. Illgen, A. Thomas and P. Strasser, *Physical Chemistry Chemical Physics*, 2012, **14**, 6444-6447.
20. P. Kichambare, J. Kumar, S. Rodrigues and B. Kumar, *Journal of Power Sources*, 2011, **196**, 3310-3316.
21. I. Yamanaka, T. Onizawa, S. Takenaka and K. Otsuka, *Angewandte Chemie International Edition*, 2003, **42**, 3653-3655.
22. R. Jasinski, *Nature*, 1964, **201**, 1212-1213.
23. J. P. Dodelet, in *N4-Macrocyclic Metal Complexes*, eds. J. H. Zagal, F. Bedioui and J. P. Dodelet, Springer, New York, 2006, pp. 83-148.
24. H. Schulenburg, S. Stankov, V. Schünemann, J. Radnik, I. Dorbandt, S. Fiechter, P. Bogdanoff and H. Tributsch, *The Journal of Physical Chemistry B*, 2003, **107**, 9034-9041.
25. A. Widelöv and R. Larsson, *Electrochimica Acta*, 1992, **37**, 187-197.
26. H. Jahnke, M. Schönborn and G. Zimmermann, *Topics in Current Chemistry*, 1976, **61**, 133-181.
27. S. Gupta, D. Tryk, I. Bae, W. Aldred and E. Yeager, *J Appl Electrochem*, 1989, **19**, 19-27.
28. K. Gong, F. Du, Z. Xia, M. Durstock and L. Dai, *Science*, 2009, **323**, 760-764.
29. J. A. R. van Veen, H. A. Colijn and J. F. van Baar, *Electrochimica Acta*, 1988, **33**, 801-804.
30. H. Wang, R. Côté, G. Faubert, D. Guay and J. P. Dodelet, *The Journal of Physical Chemistry B*, 1999, **103**, 2042-2049.
31. P. H. Matter, L. Zhang and U. S. Ozkan, *Journal of Catalysis*, 2006, **239**, 83-96.
32. P. Matter and U. Ozkan, *Catal Lett*, 2006, **109**, 115-123.
33. F. Jaouen, M. Lefèvre, J.-P. Dodelet and M. Cai, *The Journal of Physical Chemistry B*, 2006, **110**, 5553-5558.
34. Y. Okamoto, *Applied Surface Science*, 2009, **256**, 335-341.
35. R. A. Sidik, A. B. Anderson, N. P. Subramanian, S. P. Kumaraguru and B. N. Popov, *The Journal of Physical Chemistry B*, 2006, **110**, 1787-1793.
36. A. Lu, A. Kiefer, W. Schmidt and F. Schüth, *Chemistry of Materials*, 2003, **16**, 100-103.
37. A. B. Fuertes and T. A. Centeno, *Journal of Materials Chemistry*, 2005, **15**, 1079-1083.
38. S. Shrestha and W. E. Mustain, *Journal of the Electrochemical Society*, 2010, **157**, B1665-B1672.
39. A. B. Fuertes, *Microporous and Mesoporous Materials*, 2004, **67**, 273-281.
40. A. B. Fuertes, *Chemistry of Materials*, 2004, **16**, 449-455.
41. M. Kruk, M. Jaroniec and A. Sayari, *Langmuir*, 1997, **13**, 6267-6273.
42. A. B. Fuertes and D. M. Nevskaya, *Microporous and Mesoporous Materials*, 2003, **62**, 177-190.
43. M. Sevilla and A. B. Fuertes, *Carbon*, 2006, **44**, 468-474.
44. J.-S. Choi, W. S. Chung, H. Y. Ha, T.-H. Lim, I.-H. Oh, S.-A. Hong and H.-I. Lee, *Journal of Power Sources*, 2006, **156**, 466-471.
45. T. C. Nagaiah, S. Kundu, M. Bron, M. Muhler and W. Schuhmann, *Electrochemistry Communications*, 2010, **12**, 338-341.
46. H.-S. Oh, J.-G. Oh, W. H. Lee, H.-J. Kim and H. Kim, *International Journal of Hydrogen Energy*, 2011, **36**, 8181-8186.